Crackling versus Continuumlike Dynamics in Brittle Failure

J. Barés, L. Barbier, and D. Bonamy*

CEA, IRAMIS, SPCSI, Group Complex Systems and Fracture, F-91191 Gif sur Yvette, France

(Received 26 February 2013; published 31 July 2013)

We study how the loading rate, specimen geometry, and microstructural texture select the dynamics of a crack moving through an heterogeneous elastic material in the quasistatic approximation. We find a transition, fully controlled by two dimensionless variables, between dynamics ruled by continuum fracture mechanics and crackling dynamics. Selection of the latter by the loading, microstructure, and specimen parameters is formulated in terms of scaling laws on the power spectrum of crack velocity. This analysis defines the experimental conditions required to observe crackling in fracture. Beyond failure problems, the results extend to a variety of situations described by models of the same universality class, e.g., the dynamics in wetting or of domain walls in amorphous ferromagnets.

DOI: 10.1103/PhysRevLett.111.054301 PACS numbers: 46.50.+a, 62.20.M−, 78.55.Qr

Many systems, including ferromagnets [1], plastically deformed metals [2], fault seismicity [3], liquid spreading [4], and fracturing solids [5,6], crackle, i.e., respond to a slowly varying external parameter through jerky dynamics, with discrete pulses or avalanches spanning a variety of scales. The salient feature of such crackling dynamics is to exhibit universal scale-free statistics and scaling laws, independent of both microscopic details and external conditions (see Ref. [7] for a review). Those are set by generic properties such as symmetries, dimensions, and interaction range. This behavior, reminiscent of self-organized criticality, is generally explained as being due to the presence of a critical point and a mechanism attracting the system toward this point [8].

In brittle failure problems, the crack front can be identified with a long-range elastic spring [9–12], and the crack onset in heterogeneous or amorphous solids can be mapped to a critical depinning transition [13–15]. In stable crack growth experiments, crackling dynamics are sometimes observed [16] and can be attributed to a self-adjustment of the driving force around its depinning value [17]. This model is found to reproduce the scaling laws and scale-free statistics observed experimentally in Ref. [16]. Still, many situations involving a variety of disordered brittle solids (structural glasses, brittle polymers, ceramics, etc.) do not exhibit crackling. Rather, they exhibit continuous dynamics compatible with the linear elastic fracture mechanics (LEFM) predictions.

By investigating theoretically and numerically crack propagation in elastic disordered media, we reveal that either LEFM-like or crackling dynamics can be observed. A transition line is exhibited between the two regimes and defines a phase diagram within a space defined by two reduced variables that intimately mingle the specimen thickness, specimen geometry, loading rate, material constants (fracture energy and crack front mobility), and microstructural texture (disorder contrast and length scale). Within the crackling phase, the Fourier spectrum of the crack velocity is characterized by a power law with a universal exponent. Conversely, the prefactor and the two cutoffs associated with this power law are found to depend on the loading, microstructure, and specimen parameters according to scaling laws that are uncovered herein. These results are discussed within the framework of the depinning theory [18]. They shed light on the experimental conditions required to observe crackling in brittle fracture. Beyond crack growth problems, they can be immediately extended to a number of others systems described by the same long-range string model, such as the dynamics of contact lines in wetting [19] or that of magnetic domain walls with dipolar interactions [20].

Theory.—In brittle failure problems, crack destabilization and further propagation are governed by the balance between the amount of elastic energy G released by the solid as the crack propagates over a unit length and the fracture energy Γ dissipated in the fracture process zone to create two new fracture surfaces of unit area [21]. In standard continuum fracture theory, G depends on the imposed loading and specimen geometry and Γ is a material constant. In the slow fracture regime, the crack velocity v is given by $v/\mu = G - \Gamma$, where (in a perfectly linear elastic material and in the absence of any environmental effect) the effective mobility μ can be related to the Rayleigh wave speed c_R through $\mu = c_R/\Gamma$.

Defects and inhomogeneities at the microstructure scale yield fluctuations in the local fracture energy: $\Gamma(x, y, z) = \bar{\Gamma} + \gamma(x, y, z)$, where the $\hat{x}$, $\hat{y}$, and $\hat{z}$ axes are aligned with the direction of crack propagation, tensile loading, and mean crack front, respectively. This induces $(\hat{x}, \hat{z})$ in-plane and $(\hat{y}, \hat{z})$ out-of-plane distortions of the front which, in turn, generate local variations in G. To the first order, variations of G depend on the in-plane front distortion only. Thus, the problem reduces to that of a planar crack [22,23]. One can then use Rice's analysis [24] to relate the local value $G(z, t)$ of energy release to the planar front shape $f(z, t)$ (see Ref. [25] for a recent

review). Once injected in the equation of motion, this yields [26]

$$\frac{1}{\mu}\frac{\partial f}{\partial t} = F(\bar{f}, t) - \bar{\Gamma} J(z, \{f\}) + \gamma(z, x = f(z, t)), \quad (1)$$

where the long-range kernel J is more conveniently defined by its z-Fourier transform $\hat{J}(q) = -|q|\hat{f}$. Here, $F(\bar{f}, t) = G(\bar{f}, t) - \bar{\Gamma}$ and $G(\bar{f}, t)$ denotes the mechanical energy release which would result from the same loading conditions with a straight crack front at the mean position $\bar{f}(t) = \langle f(z, t)\rangle_z$. This equation is that of a long-range elastic line driven by this force F within the frozen random potential $\gamma(z, x)$. It exhibits a depinning transition at a critical value F_c, characterized by avalanche dynamics and universal scale-free behaviors [19].

The function $G(\bar{f}, t)$ is selected by the specimen geometry and imposed loading. It has to be determined using LEFM. In stable growth situations, it should increase with t (crack loaded by imposing external displacements that grow with t) and decreases with $\bar{f}$ (specimen compliance increases with f). Without loss of generality, we consider an immobile crack at $t = 0$ and we set the x-axis origin at its tip [$\bar{f}(t=0)=0$]. Then, one gets $G(\bar{f} = 0, t = 0) = \bar{\Gamma}$. Considering the subsequent variations $f(z, t)$ are small with respect to the initial crack length, one can write

$$F(\bar{f}, t) = \dot{G}t - G'\bar{f}, \quad (2)$$

where $\dot{G} = \partial G/\partial t$ (driving rate) and $G' = -\partial G/\partial \bar{f}$ (unloading factor) are positive constants set by the imposed displacement rate and the specimen geometry, respectively.

To complete the description, one finally has to make the random term γ precise in Eq. (1). *A priori*, this latter is characterized by the probability function $p(\gamma)$ and the spatial correlation function $C(\vec{r}) = \langle\gamma(\vec{r}_0 + \vec{r})\gamma(\vec{r}_0)\rangle_{r_0}$. In the following, we will consider (i) a Gaussian distribution p of standard deviation $\tilde{\gamma}$ and (ii) an isotropic correlation function C that decreases linearly with $|r|$ over a distance ℓ (correlation length for the disorder landscape) beyond which $C = 0$. Note that the scaling properties are expected to remain unaffected by changing the shapes $p(\gamma)$ and $C(|r|)$ [27]. Microstructural disorder is then fully characterized by $\tilde{\gamma}$ and ℓ.

In this framework, the front dynamics are *a priori* set by seven parameters: μ, $\bar{\Gamma}$, $\dot{G}$, G', $\tilde{\gamma}$, ℓ, and the system size L (specimen thickness along the z axis). By introducing the dimensionless time $t \to t/(\ell/\mu\bar{\Gamma})$ and length $\{x, z, f\} \to \{x/\ell, z/\ell, f/\ell\}$, one gets

$$\frac{\partial f}{\partial t} = ct - k\bar{f} - J(z, \{f\}) + \eta(z, x = f(z, t)), \quad (3)$$

where $c = \dot{G}\ell/\mu\bar{\Gamma}^2$ is the dimensionless driving rate, $k = G'\ell/\bar{\Gamma}$ is the dimensionless unloading factor, and η is a Gaussian random term of standard deviation $\sigma = \tilde{\gamma}/\bar{\Gamma}$ and unit spatial correlation length. As a result, the front dynamics are selected by only four independent parameters: c, k, σ, and the scale ratio $N = L/\ell$.

Numerics.—Using a fourth order Runge-Kutta scheme, we solved Eq. (3) for a front $f(z, t)$ propagating in an $N \times pN$ uncorrelated random Gaussian map $\eta(z, x)$ with zero average and σ variance [p sets the $(\hat{x}, \hat{z})$ aspect ratio]. The parameter c was varied from 10^{-6} (imposed by the time limit of 40 days on a 2 GHz CPU we impose for each simulation) to 10^{-4} (to keep a large enough scale separation between the depinned front velocity and the loading rate). The parameters k, σ, and N were respectively varied from 10^{-8} to 1, 10^{-1} to 4, and 32 to 2048. This permits a wide exploration of the phase diagram (eight decades in the relevant units; see Fig. 2 and the associated text).

Results.—The left panel of Fig. 1, showing A_1, A_2, and A_3, presents typical time profiles of the spatially averaged crack velocity $\bar{v}(t) = d\bar{f}/dt$ for constant c and increasing k. At low k, $\bar{v}(t)$ fluctuates over the mean value c/k that would have been expected from continuum mechanics (CM), i.e., for $\eta = \gamma \equiv 0$. When k increases, the signal becomes more jerky and, above a given value, exhibits crackling dynamics, with distinct pulses separated by silent periods where $\bar{v} = 0$. The transition k_c between these two regimes can be computed by plotting the minimum value of $\bar{v}(t)$ as a function of k (right panel of Fig. 1). $v_{\min}$ is equal to zero in the crackling regime and increases with k in the CM-like regime, above k_c.

In the inset of Fig. 2(a), we plot k_c vs c as measured in systems of fixed $p = 3$ and various N and σ. A c-independent plateau $k_{c\,\mathrm{sat}}$ is observed at low c, low N, and large σ while k_c increases linearly (slope A) with c at high c, high N, and low σ. All curves can then be superimposed by making $k_c \to k_c^* = k_c/k_{c\,\mathrm{sat}}$ and $c \to c^* = Ac/k_{c\,\mathrm{sat}}$. Both A and $k_{c\,\mathrm{sat}}$ are found to go as a power

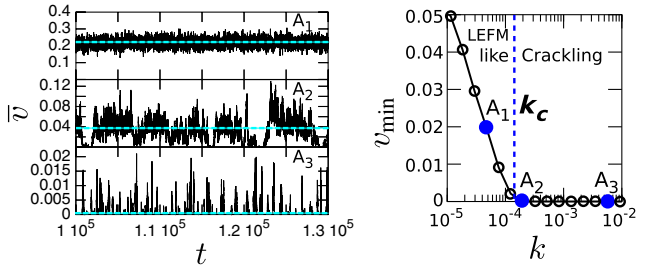

FIG. 1 (color online). Left panel: Time evolution of the spatially averaged crack front velocity $\bar{v}(t)$ for increasing unloading factor k: $k = 4.75 \times 10^{-5}$ (A_1), $k = 2 \times 10^{-4}$ (A_2), and $k = 5.5 \times 10^{-3}$ (A_3). Other parameters are kept as constants: $c = 10^{-5}$, $N = 1024$, and $\sigma = 1$. At low k, $\bar{v}(t)$ wanders around the value c/k expected in the absence of microstructural disorder, with relative fluctuations that decrease with k. For higher k, the dynamics become jerky and, above a given value k_c, separated pulses can be distinguished, which sharpen as k increases. Right panel: Minimum value of $\bar{v}(t)$ vs k. The transition value k_c between CM-like and crackling dynamics is precisely defined as the smallest value k for which $v_{\min} = 0$.

law with N and σ: $A \approx \sigma^{-\alpha_1} N^{\alpha_2}$ with $\alpha_1 = 1.15 \pm 0.05$ and $\alpha_2 = 0.38 \pm 0.05$, and $k_{c\,\mathrm{sat}} \approx \sigma N^{-\alpha_3}$ with $\alpha_3 = 1.65 \pm 0.05$. The resulting master function, plotted in Fig. 2(a) (main), is

$$k_c^* = f(c^*), \qquad f(c^*) \approx \begin{cases} k_{c\,\mathrm{sat}}^* & \text{if } c^* \ll k_{c\,\mathrm{sat}}^* \\ c^* & \text{if } c^* \gg k_{c\,\mathrm{sat}}^*, \end{cases} \tag{4}$$

where $c^* = c \times N^{\alpha_2+\alpha_3}/\sigma^{1+\alpha_1}$ and $k_c^* = k_c/\sigma N^{-\alpha_3}$. The plateau value $k_{c\,\mathrm{sat}}^*$ is found to decrease with p. This curve separates CM-like and crackling dynamics.

The form of the k_c vs c curves can be understood by analyzing the profile $\eta^{\mathrm{eff}}(x) = \langle J(z,\{f\}) + \eta[z, x = f(z,t)]\rangle_z$ of the effective pinning force applying on the front as it propagates throughout the disordered landscape. Such a profile is depicted in Fig. 2(b). The value $k_{c\,\mathrm{sat}}$ observed for $c \to 0$ is set by the relative positions of the maximum and the following next-to-maximum peaks over the traveled distance [$S_1 = \{x_1, \eta_1\}$ and $S_2 = \{x_2, \eta_2\}$ in Fig. 2(b)]: $k_{c\,\mathrm{sat}} = (\eta_1 - \eta_2)/(x_2 - x_1)$. At finite c, the front earns an extra driving force during its depinning jump (duration τ_{12}) from S_1 to S_2, yielding $k_c = k_{c\,\mathrm{sat}} + Ac$ with $A = \tau_{12}/(x_2 - x_1)$. One thus expects $k_c \approx k_{c\,\mathrm{sat}}$ for $c \ll k_{c\,\mathrm{sat}}/A$ and $k_c \approx Ac$ for $c \gg k_{c\,\mathrm{sat}}/A$. The linear variation of $\{\eta^{\mathrm{eff}}\}$ with σ explains the observed $k_{c\,\mathrm{sat}} \propto \sigma$.

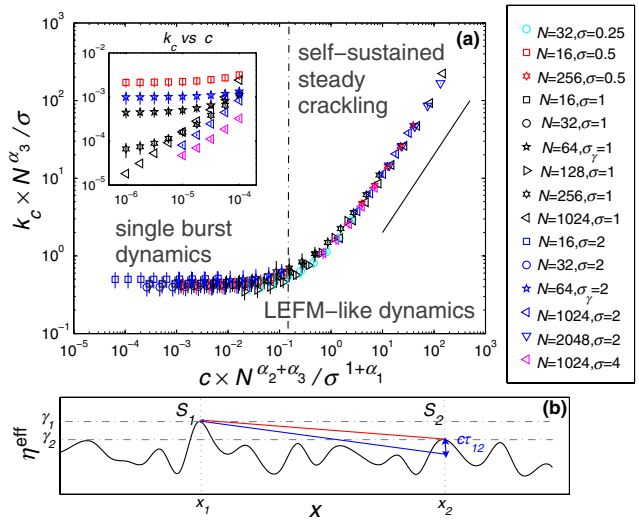

FIG. 2 (color online). (a) Phase diagram of the crack dynamics. Inset: Variation of k_c as a function of c for different N and σ (values on the right-hand side). Each point results from averaging over many simulations, and the error bars correspond to a 95% confidence interval. Main panel: Collapse obtained using Eq. (4) with $\alpha_1 = 0.38$, $\alpha_2 = 1.15$, and $\alpha_3 = 1.65$. The straight line indicates proportionality. In both graphs, the axes are logarithmic. (b) Sketch of the variation of the effective pinning force applying on the front as it quasistatically propagates throughout the disordered landscape (see, e.g., Ref. [35] for implementation of such a propagation algorithm). Points $S_1 = \{x_1, \eta_1\}$ and $S_2 = \{x_2, \eta_2\}$ locate the maximum and following next-to-maximum peaks over the traveled distance (see the text for details).

Note that in this scenario, the jerky dynamics observed for $c \ll k_{c\,\mathrm{sat}}/A$ are dominated by a single large avalanche (from S_1 to S_2), while true steady self-sustained crackling dynamics can only be observed for $c \gg k_{c\,\mathrm{sat}}/A$.

We now focus on the evolution of the fracturing dynamics $\bar{v}(t)$ within the steady regimes of the phase diagram. One way to characterize it is to analyze its power spectrum (PS). Such an analysis, indeed, has two advantages with respect to the standard statistical analysis of pulse size and duration developed to analyze crackling signals [28]: (i) it allows a full exploration of the phase diagram (both crackling and CM-like), and (ii) in the crackling part, it does not call for any additional criteria (threshold setting) to filter single pulses in the presence of overlapping avalanches. Figure 3 presents the evolution of PS(ν) for increasing k and the other parameters constant. Below k_c, all curves overlap except at the lowest frequencies. This is precisely what is requested in a CM description, where the continuum-level scale control parameter k should affect the system at large scales only. Conversely, above k_c, the PS curves are distinct, showing that all scales are affected by k. One points out the power law behavior characteristic of crackling dynamics [28–30]. The power law exponent $1/a$ is independent of k, whereas the prefactor decreases with k. The dramatic change observed as k crosses k_c is a signature that the CM-crackling transition line is a true transition, not a crossover phenomenon.

We turn now to the quantitative selection of the PS in the crackling regime. The curve collapse presented in Fig. 4(a) unravels the scaling between the power law prefactor and the series of variables c, k, and N: Over the range $\nu_{\min} \leq \nu \leq \nu_{\max}$, PS($\nu$) is

$$\mathrm{PS} \approx \frac{\sigma^{2\kappa}}{N}\frac{c}{k}\nu^{-1/a}. \tag{5}$$

The upper cutoff is found to depend on σ only [Fig. 4(b), inset], while the lower one depends on k only [Fig. 4(b), main]:

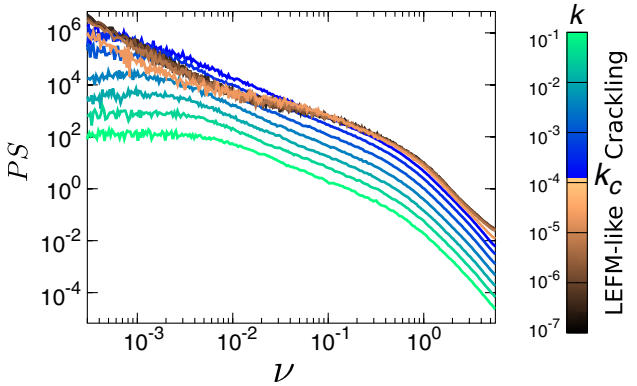

FIG. 3 (color online). PS of $\bar{v}(t)$ obtained for various values of k (logarithmic axes). Other parameters are kept constant: $c = 10^{-5}$, $N = 1024$, and $\sigma = 1$. The colorbar on the right indicates the k value. Note the qualitative change at the transition k_c and the power law observed above in the crackling regime.

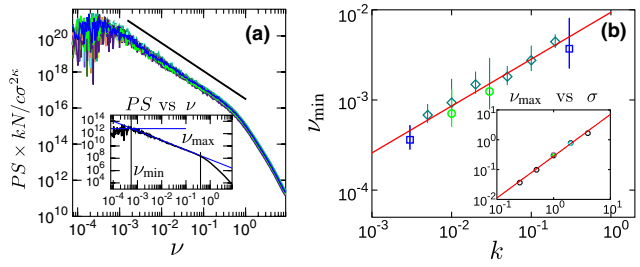

FIG. 4 (color online). (a), main panel: Collapsed PS curves of $\bar{v}(t)$ in the self-sustained steady crackling part of the phase diagram (logarithmic axes). The collapse is obtained using Eq. (5) with $\kappa = 0.7$. The different curves (with different colors) correspond to different values of c, k, N, σ: $10^{-6} \leq c \leq 3 \times 10^{-4}$, $3 \times 10^{-3} \leq k \leq 3 \times 10^{-2}$, $128 \leq N \leq 2048$, $\sigma = 1$. The straight black line is a power law of exponent $1/a = 1.5$. (a), inset: For a given PS(ν) curve, ν_{min} is defined from the intersection of the power law and the plateau value at low frequencies, while ν_{max} sets the upper cutoff for the power law. (b), main panel: Variation of the lower cutoff ν_{min} with k for $c = 10^{-5}$ (circles), $c = 3 \times 10^{-5}$ (rectangles), $c = 3 \times 10^{-5}$ (diamonds), and constant values $N = 1024$ and $\sigma = 1$ (it was checked that ν_{min} is independent of both N and σ). (b), inset: Variation of the upper cutoff ν_{max} with σ for $N = 128$ (rectangles), $N = 256$ (triangle), $N = 1024$ (circles), $N = 2048$ (diamonds), and constant values $c = 10^{-5}$ and $k = 10^{-3}$ (it was checked that ν_{max} is independent of both c and k). In both plots, straight lines are power laws [Eq. (6)] with $2\kappa = 1.4$ and $\Delta = 0.52$.

$$\nu_{max} \approx \sigma^{2\kappa}, \qquad \nu_{min} \approx k^{\Delta}. \tag{6}$$

In Eqs. (5) and (6), the fitted exponents were found to be $1/a \simeq 1.50 \pm 0.02$, $\kappa \simeq 0.7 \pm 0.1$, and $\Delta \simeq 0.52 \pm 0.08$.

Discussion.—The crackling pulses evidenced in the $\bar{v}(t)$ signal result from the depinning avalanches. Single, non-overlapping avalanches are known to exhibit universal scale-free distributions and scaling relations characterized by a variety of critical exponents, which can be estimated using renormalization group [18,19] or numerical [31,32] methods. These scale-free features only hold for length scales larger than the Larkin length [33] L_c, which, for our model, scales as $L_c \approx 1/\sigma^2$. We then expect $\nu_{max} \approx 1/L_c^{\kappa} \approx \sigma^{2\kappa}$, where $\kappa = 0.770(5)$ [32] refers to the dynamic exponent. This value is in agreement with that measured here. In the so-called adiabatic limit ($c \to 0$), there is a one-to-one relation between the $\bar{v}(t)$ pulses and the single depinning avalanches. Then, the PS exponent a_{ad} in Eq. (5) (here, the "ad" index stands for "adiabatic limit") is expected [29] to be the one that defines the scaling $T \propto S^{a_{ad}}$ between the avalanche size S and duration T: $a_{ad} = \kappa/(1 + \zeta)$ [5], where $\zeta = 0.385(5)$ [31,32] refers to the roughness exponent. As a result, one expects $1/a_{ad} = 1.80(2)$. The exponent Δ_{ad} in Eq. (6) defines the scaling between the upper cutoff in time for scale-free features and the unloading factor k. In our model, it is given by $\Delta_{ad} = \kappa/2$ [5], which yields $\Delta_{ad} = 0.385(5)$. Both Δ_{ad} and $1/a_{ad}$ are found to be significantly different from the values Δ and a measured herein. By yielding some overlap between the avalanches, a finite driving rate c, indeed, is expected [34] to alter the PS shape and the cutoff dependencies. It is interesting to note that the effect is limited to a novel value set for a and Δ, without modifying the power law shape for PS or yielding an additional dependency with c for ν_{min}. By yielding percolation throughout the space-time diagram as c increases and/or k decreases, the overlap effect is also believed to drive the crackling-CM transition. Ongoing work aims at accurately characterizing this coalescence process. This will allow unraveling the selection of a and Δ in Eq. (5) and that of α_i in Eq. (4).

To summarize, we have analyzed here how a brittle crack selects its propagation dynamics in the presence of microstructural disorder. Large disorder (contrast or length scale), large unloading factor, small specimen size, and small driving rate yield crackling dynamics, while the opposite yields CM-like dynamics. The associated phase diagram is unraveled and is shown to be fully controlled by two reduced variables [Fig. 2 and Eq. (4)] that intimately mingle the above parameters. Relations between these parameters and the dynamics in the crackling phase (the Fourier spectrum of the crack velocity) have finally been determined [Eqs. (5) and (6)].

This work sheds light on the experimental conditions required to observe crackling in brittle fracture. It also provides insights on how to decipher the crackling dynamics and gain information on the underlying conditions, e.g., in terms of microstructure or loading when those are not *a priori* known. These results can also inform technological relevant fracture processes, e.g., in the future development of rationalized design methodologies to prevent (or to limit) inopportune crackling (and induced indetermination) in cutting technologies. Beyond solid failure, our analysis directly extends to a number of other systems described by the same long-range string model, such as the dynamics of contact lines in wetting problems [19] and the dynamics of domain walls in ferromagnets [20] (the field sweep rate and the demagnetization factor then playing the roles of c and k). As such, it may be relevant to other fields facing similar problems, e.g., nanofluidic or nanomagnetism technologies.

We thank Alberto Rosso and Alexander Dobrinevski for fruitful discussions and Cindy Rountree for a critical reading of this manuscript. Support through the ANR project MEPHYSTAR is gratefully acknowledged.

*Corresponding author.
daniel.bonamy@cea.fr

[1] S. Papanikolaou, F. Bohn, R. L. Sommer, G. Durin, S. Zapperi, and J. P. Sethna, Nat. Phys. **7**, 316 (2011).
[2] T. Richeton, J. Weiss, and F. Louchet, Nat. Mater. **4**, 465 (2005).

[3] J. B. Rundle, D. L. Turcotte, R. Shcherbakov, W. Klein, and C. Sammis, Rev. Geophys. **41**, 1019 (2003).
[4] R. Planet, S. Santucci, and J. Ortin, Phys. Rev. Lett. **102**, 094502 (2009).
[5] D. Bonamy, J. Phys. D **42**, 214014 (2009).
[6] J. Rosti, X. Illa, and J. K. M. J. Alava, J. Phys. D **42**, 214013 (2009).
[7] J. P. Sethna, K. A. Dahmen, and C. R. Myers, Nature (London) **410**, 242 (2001).
[8] R. Dickman, M. A. Munoz, A. Vespignani, and S. Zapperi, Braz. J. Phys. **30**, 27 (2000).
[9] H. Gao and J. R. Rice, J. Appl. Mech. **56**, 828 (1989).
[10] J. Schmittbuhl, S. Roux, J. P. Vilotte, and K. J. Måløy, Phys. Rev. Lett. **74**, 1787 (1995).
[11] S. Ramanathan, D. Ertas, and D. S. Fisher, Phys. Rev. Lett. **79**, 873 (1997).
[12] D. Bonamy, L. Ponson, S. Prades, E. Bouchaud, and C. Guillot, Phys. Rev. Lett. **97**, 135504 (2006).
[13] S. Roux, D. Vandembroucq, and F. Hild, Eur. J. Mech. A. Solids **22**, 743 (2003).
[14] L. Ponson, Phys. Rev. Lett. **103**, 055501 (2009).
[15] D. Bonamy and E. Bouchaud, Phys. Rep. **498**, 1 (2011).
[16] K. J. Måløy, S. Santucci, J. Schmittbuhl, and R. Toussaint, Phys. Rev. Lett. **96**, 045501 (2006).
[17] D. Bonamy, S. Santucci, and L. Ponson, Phys. Rev. Lett. **101**, 045501 (2008).
[18] P. Chauve, P. Le Doussal, and K. J. Wiese, Phys. Rev. Lett. **86**, 1785 (2001).
[19] D. Ertas and M. Kardar, Phys. Rev. E **49**, R2 532 (1994).
[20] G. Durin and S. Zapperi, Phys. Rev. Lett. **84**, 4705 (2000).
[21] L. B. Freund, *Dynamic Fracture Mechanics* (Cambridge University Press, Cambridge, England, 1990).
[22] R. C. Ball and H. Larralde, Int. J. Fract. **71**, 365 (1995).
[23] A. B. Movchan, H. Gao, and J. R. Willis, Int. J. Solids Struct. **35**, 3419 (1998).
[24] J. R. Rice, J. Appl. Mech. **52**, 571 (1985).
[25] V. Lazarus, J. Mech. Phys. Solids **59**, 121 (2011).
[26] L. Ponson and D. Bonamy, Int. J. Fract. **162**, 21 (2010).
[27] D. Vandembroucq, R. Skoe, and S. Roux, Phys. Rev. E **70**, 051101 (2004).
[28] A. Travesset, R. A. White, and K. A. Dahmen, Phys. Rev. B **66**, 024430 (2002).
[29] M. C. Kuntz and J. P. Sethna, Phys. Rev. B **62**, 11 699 (2000).
[30] G. Durin and S. Zapperi, in *The Science of Hysteresis*, edited by G. Bertotto and I. Mayergoyz (Academic, New York, 2005), p. 181.
[31] A. Rosso and W. Krauth, Phys. Rev. E **65**, 025101(R) (2002).
[32] O. Duemmer and W. Krauth, J. Stat. Mech. (2007) P01019.
[33] A. I. Larkin and Y. N. Ovchinnikov, J. Low Temp. Phys. **34**, 409 (1979).
[34] R. A. White and K. A. Dahmen, Phys. Rev. Lett. **91**, 085702 (2003).
[35] A. Tanguy, M. Gounelle, and S. Roux, Phys. Rev. E **58**, 1577 (1998).